Available online at www.sciencedirect.com
ScienceDirect
Acta Materialia 58 (2010) 4233–4244
Acta MATERIALIA
www.elsevier.com/locate/actamat

Constrained sintering of an air-plasma-sprayed thermal barrier coating

A.C.F. Cocks [a,*], N.A. Fleck [b]

[a] Department of Engineering Science, Parks Rd., Oxford OX1 3PJ, UK
[b] Cambridge University Engineering Department, Trumpington St., Cambridge CB2 1PZ, UK

Received 5 October 2009; received in revised form 26 February 2010; accepted 8 April 2010
Available online 13 May 2010

Abstract

A micromechanical model is presented for the constrained sintering of an air-plasma-sprayed, thermal barrier coating upon a thick superalloy substrate. The coating comprises random splats with intervening penny-shaped cracks. The crack faces make contact at asperities, which progressively sinter in-service by interfacial diffusion, accommodated by bulk creep. Diffusion is driven by the reduction in interfacial energy at the developing contacts and by the local asperity contact stress. At elevated operating temperature, both sintering and creep strains accumulate within the plane of the coating. The sensitivities of sintering rate and microstructure evolution rate to the kinetic parameters and thermodynamic driving forces are explored. It is demonstrated that the sintering response is governed by three independent timescales, as dictated by the material and geometric properties of the coating. Finally, the role of substrate constraint is assessed by comparing the rate of constrained sintering with that for free sintering.

Keywords: Sintering; Coatings; Variational methods; Micromechanical modelling; Creep

1. Introduction

Air-plasma-sprayed (APS) thermal barrier coatings (*TBC*s) are increasingly used to give thermal and environmental protection of non-rotating components in gas turbines. The APS coating is deposited as liquid droplets and upon striking the substrate these droplets are rapidly solidified to pancake-shaped polycrystals, termed "splats". The gaps between splats resemble penny-shaped cracks, and under high temperature service conditions these cracks sinter together at discrete contact points, giving rise to a deleterious increase in both Young's modulus and thermal conductivity [1–4]. Sintering is driven both by in-plane stress within the coating and by the surface energy $\gamma_{TBC} \approx 1$ J m^{-2} of the zirconia.

Recently, Fleck and Cocks [5] have developed a sintering model for APS material. They assumed a random, 3D distribution of penny-shaped cracks and they accounted for sintering at the discrete asperity contacts across the faces of each crack, accommodated by bulk creep. This constitutive description is used in the current study to explore the role of substrate constraint upon the sintering response. The Fleck and Cocks [5] model includes the feature that the *TBC* increases in modulus as sintering progresses, due to the increase in size and contact stiffness of the asperities. This increase in modulus is of practical relevance, as a high modulus promotes high in-plane stresses within the coating during thermal cycling and this can promote delamination. Experimental data confirm that asperity sintering leads to an increase in modulus for both freely supported and constrained films. Some examples are given as follows.

The Young's modulus of the as-deposited coating is in the range 10–50 GPa [2,4,6,7], with the exact value depending upon the details of the processing condition and microstructure created. When the free-standing coating is held at an elevated temperature to represent in-service conditions, the modulus first increases rapidly with time. The rate then slows, and for temperatures less than about 1320 °C, a plateau is generally observed over the timescale of the experiment [2,4]. For example, Choi et al. [2] observed an

* Corresponding author. Tel.: +44 1865 283490; fax: +44 1865 273906.
E-mail address: alan.cocks@eng.ox.ac.uk (A.C.F. Cocks).

1359-6454/$36.00 © 2010 Acta Materialia Inc. Published by Elsevier Ltd. All rights reserved.
doi:10.1016/j.actamat.2010.04.015

Nomenclature

Symbols

b	asperity top diameter
D	diffusion constant
f	dimensionless damage parameter
E	Young's modulus
G	Gibbs' free energy
j	volumetric flux
k	asperity contact stiffness
K	bulk modulus
ℓ	side length of asperity
N	number of cracks per unit volume
s	asperity spacing or deviatoric stress
R	crack radius
$\bar{R}$	representative crack radius
t	time
T	traction
u	displacement due to asperity deformation
U	strain energy density
v	crack opening displacement
w	asperity height

Greek symbols

α	linear coefficient of thermal expansion
β	inclination angle of asperity
Δ	change
χ	damage parameter
ε	strain
γ	interfacial energy
η	viscosity
λ	asperity bottom diameter
μ	shear modulus
ν	Poisson's ratio
Θ	temperature
σ	stress
τ	time constant
Ω	overall rate functional
Ψ	rate potential

Superscript

∞	remote

Subscripts

0	initial value or reference value
C	creep
D	deposition
E	elastic
eff	effective
G	grain boundary
h	hydrostatic
S	substrate or surface
T	thermal
TBC	thermal barrier coating
Y	flow strength

increase from 25 GPa to a plateau of 75 GPa after 100 h at 1316 °C, while Lampenscherf [7] reports an increase from 40 GPa to 80 GPa over the same timescale at 1270 °C. Both these plateau values are much less than the modulus (219 GPa) of the fully dense material. Thompson and Clyne [4] observed that, during the initial rapid stage of modulus increase, asperities come into contact and junctions develop across the faces of the intersplat cracks. At high temperatures (on the order of 1400 °C) this initial stage of sintering is followed by healing of the interspat cracks and thereby to a progressive increase in modulus. Similar microstructural changes have been observed in creep and sintering experiments by Soltani et al. [8].

Thompson and Clyne [4] also examined the sintering response of a coating constrained by a substrate. The constraint led to a slower rate of increase of modulus compared with the free sintering case. Subsequently, Cipitria et al. [9,10] made a theoretical assessment of the significance of substrate constraint upon the sintering response. Similar experimental and theoretical studies on the role of substrate constraint have been conducted by Bordia and Jagota [11] and Guillon et al. [12] for particulate systems and by Hutchinson et al. [13] for ePVD thermal barrier coatings. In each case, the constraint imposed by the substrate slows the rate of sintering compared with that experienced during free sintering. In the present study, the role of substrate constraint is explored theoretically by extending the Fleck and Cocks model [5] to the case of constrained sintering.

The Fleck and Cocks [5] model is based upon the notion that a change in free energy drives dissipative processes such as Coble creep and diffusion on the asperity scale. By writing the free energy (and a dissipation potential) in terms of a small number of degrees of freedom, such as asperity size and shape, the evolution of microstructure can be predicted over multiple length-scales. Thermodynamic restrictions (e.g. positive plastic work) are automatically satisfied upon introduction of the variational framework of Cocks et al. [14] and Suo [15]. A similar approach has been adopted for the sintering of APS *TBC* by Cipitria et al. [9,10]. Their idealization is essentially that of a 3D unit cell, with a single "bridge contact" bonding together adjacent splats. The diffusion distances are on the order of the splat size. Also, the macroscopic modulus is held fixed as sintering of the bridge contacts progresses. In contrast, Fleck and Cocks [5] allow diffusion to take place on both the asperity scale and the scale of the columnar grains within each splat; also, they explicitly account for the evolution of macroscopic modulus with increasing asperity size, as remarked above. We emphasize that the

change in modulus leads to a change in the driving force for sintering associated with the elastic free energy of the solid.

2. Scope of study

An assessment is made of the relative roles of the driving forces for constrained sintering of a coating arising from both the thermal mismatch strain and surface energy. The sensitivity of sintering rate to microstructural geometry and kinetic parameters is explored. And the evolution in microstructure and of Young's modulus is determined. Finally, the significance of substrate constraint is assessed by comparing the rate of constrained sintering with that for free sintering. A nomenclature of symbols used in the present study is presented in Nomenclature.

3. Microstructural features of the APS *TBC* system

The APS coating comprises an assembly of zirconia splats, with intervening cracks and porosity, see Fig. 1 of Fleck and Cocks [5], or Figs. 2 and 3 of Cipitria et al. [9]. Typically, the *TBC* layer is of thickness 300–500 μm, and sits on an aluminium-rich bond coat (BC) of thickness 150–300 μm. Each splat is about 1 μm thick, and has a diameter of 20–100 μm. The splats have a characteristic internal microstructure: they comprise columnar grains of diameter 0.1–0.2 μm. The intersplat cracks are approximately penny-shaped and of diameter 20–500 μm, with a maximum opening of 1 μm. Porosity also exists, of volume fraction about 15% and diameter 1–20 μm. The effect of voids upon the modulus and thermal conductivity is negligible, as discussed by Sevostianov et al. [16]. Therefore, in this study we focus on constrained sintering of the intersplat, penny-shaped cracks.

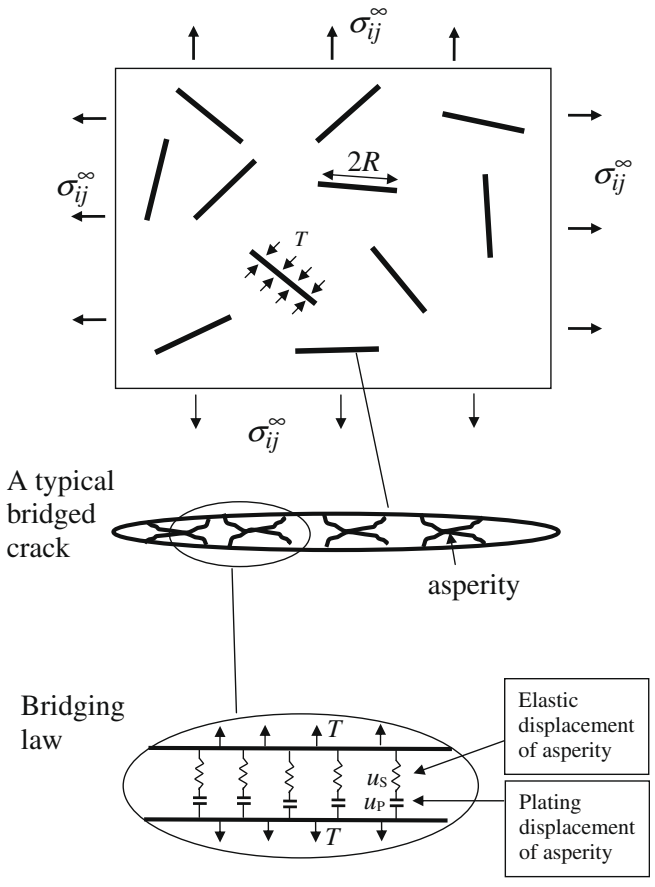

Fig. 1. The micro-cracked geometry under study. The matrix surrounding the penny-shaped cracks is elastic, linear viscous. A tensile traction T pulls the faces of each crack together, under the assumed sign convention. This tensile traction stretches the bridging asperities across the crack faces, as illustrated in the intermediate figure. The lower figure details the partitioning of crack bridging displacements into elastic and plating (sintering) components.

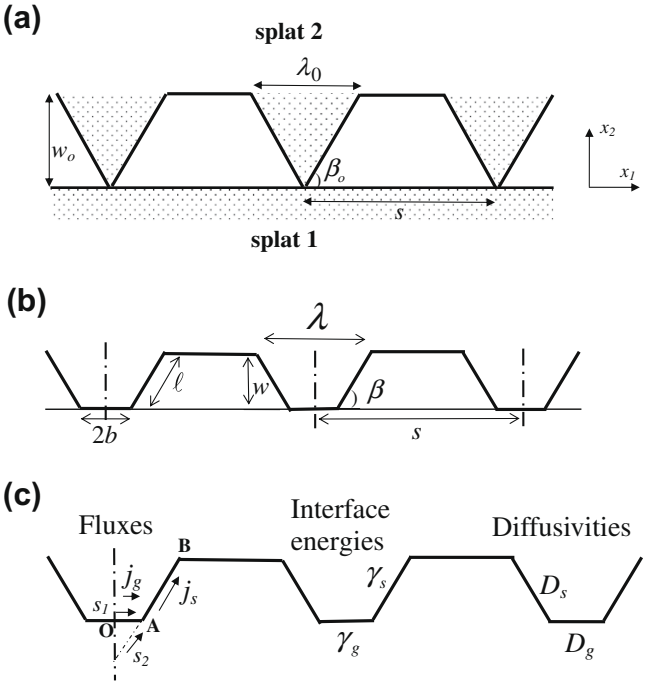

Fig. 2. The local contact geometry at asperities on the surfaces of a penny-shaped crack: (a) reference configuration; (b) typical state; (c) definition of fluxes, surface energies and diffusivities at the contacts.

4. The thermal strain within the *TBC* layer

The in-plane thermal expansion coefficient of the coating, $\alpha_{TBC} = 10 \times 10^{-6}\,\mathrm{K}^{-1}$, is independent of the degree of sintering, and is significantly less than that of the underlying nickel-based superalloy, $\alpha_S = 15 \times 10^{-6}\,\mathrm{K}^{-1}$. Assume that the *TBC* layer is in a stress-free state at the deposition temperature of $\Theta_D = 500$ °C. During operation, active cooling of the substrate limits its temperature to the order of 900 °C, and induces a temperature gradient through the *TBC* coating, such that its temperature Θ is in the range 900–1300 °C. Consequently, the thermal expansion mismatch strain ε_T varies throughout the coating and is of magnitude

$$\varepsilon_T \equiv \alpha_{TBC}(\Theta - \Theta_D) - \alpha_S(\Theta_S - \Theta_D) \quad (1)$$

For example, at the bottom of the coating ε_T is on the order of -0.2%, whereas at its top surface we have $\varepsilon_T \approx 0.2\%$. This mismatch is accommodated initially by tensile elastic strains (and stresses) within the *TBC* layer. The initial in-plane modulus of the *TBC* layer is on the order of $E_{TBC} = 40$ GPa, and so the initial thermal stress is 80 MPa at the bottom of the coating and -80 MPa at the top of the coating. Coble creep partially relaxes this in-plane stress over a timescale τ_1, as detailed below.

5. The sintering model

We begin by summarizing the pertinent features and constitutive relations of the sintering model by Fleck and Cocks [5]. In this model, the intersplat gaps of the APS coating are treated as a random distribution of penny-shaped cracks, as sketched in Fig. 1. The crack faces are in contact at asperities, and these contacts endow the faces of the cracks with a finite contact stiffness. If the contact stress on an individual asperity exceeds the indentation hardness at the operating temperature, then rate-independent plastic flow occurs and the contact area increases in order to carry the contact load. Diffusional flow also occurs at the asperity level and leads to an increase (or decrease) in the size of the contacts and thereby to changes in the contact stiffness. Simultaneously, bulk diffusional flow within the splats causes them to undergo linear viscous (Coble) creep. Thus, the constitutive description entails interfacial diffusion at the asperity level, along with bulk Coble creep, and elastic straining of the solid. The full development of the model has already been detailed by Fleck and Cocks [5]. Here, we outline the essential features of the model and specialize it to the constrained sintering case.

5.1. The physical problem

Assume that the solid contains N penny-shaped cracks per unit volume, of random orientation and random radius R. We introduce a representative radius of the penny-shaped cracks $\bar{R} \equiv \langle R^3 \rangle^{1/3}$, where the angle brackets denote an average. Then, the macroscopic bulk modulus K and shear modulus μ depend upon the dimensionless "damage parameter" $f \equiv N\langle R^3 \rangle = N\bar{R}^3$. This quantity has been measured in Ref. [16] and is of magnitude 0.4 and above. The surfaces of the cracks are rough and are in contact at the asperity level. Consequently, a traction can be transmitted across the crack faces; write the net tensile bridging traction as T (negative in value when the cracks are internally pressurized by overlapping asperities).

The roughness is on the length scale of the *TBC* columns within each splat, with a wavelength s, and is modelled by a random distribution of asperities, as follows. Each asperity that bridges the penny-shaped cracks is treated as a circular conical frustum, with top diameter $2b$, bottom diameter λ, height w, and centre–centre spacing s (as sketched in Fig. 2 of Fleck and Cocks [5]). As interfacial diffusional flow proceeds, w decreases, the contact diameter $2b$ and base diameter λ both increase and the wavelength s remains fixed.

A reference configuration for each asperity is introduced for algebraic convenience, see Fig. 2a. This configuration defines the pre-sintered state in terms of the diameter λ_0 and height w_0. However, asperity sintering occurs during both deposition and service, and so the reference state is not physically realized: the *TBC* has already partially sintered after deposition. Assume an initial state after deposition such that (w_1, λ_0) are the initial values of (w, λ). Straightforward geometrical arguments can be used to relate the contact diameter $2b$ and inclination β to the primary unknowns (w, λ); see the current configuration as sketched in Fig. 2b. Incompressibility dictates

$$2b = -\frac{\lambda}{2} + \sqrt{\lambda_0^2 \frac{w_0}{w} - \frac{3}{4}\lambda^2} \quad (2)$$

with

$$\tan\beta = \frac{2w}{\lambda - 2b} \quad (3)$$

5.2. Elastic response

Consider a micro-cracked solid as sketched in Fig. 1. The solid is loaded by the macroscopic stress σ_{ij}^{∞}, and the crack faces are subjected to a tensile normal traction T which tends to close the cracks. The Young's modulus of the cracked solid E (with no asperity bridging, $T = 0$) is related to the Young's modulus of the uncracked parent solid E_0 via a knock-down factor χ, such that

$$E = \chi E_0 \quad \text{where } \chi = 1 - \frac{16}{9} f \quad (4)$$

Similarly, the Poisson's ratio v of the cracked solid is related to the value v_0 of the uncracked solid according to

$$v = \chi v_0 \quad (5)$$

The bulk modulus K reads

$$K = \frac{E}{3(1-2v)} = \frac{\chi E_0}{3(1-2\chi v_0)} \quad (6)$$

while the shear modulus μ is

$$\mu = \frac{E}{2(1+v)} = \frac{\chi E_0}{2(1+\chi v_0)} \quad (7)$$

Asperity contact gives rise to a finite traction T on the crack faces, see Fig. 1. The macroscopic elastic strain ε_{Eij} of the cracked solid is given by

$$\varepsilon_{Eij} = \left(\frac{1+v}{E}\right)\sigma_{ij}^{\infty} - \frac{3v}{E}\sigma_h^{\infty}\delta_{ij} - \left(\frac{1-\chi}{\chi}\right)\frac{T}{E_0}\delta_{ij} \quad (8)$$

where δ_{ij} is the Kronecker delta and repeated suffices denote summation from 1 to 3 in the usual manner.

The average crack opening displacement v of the bridged penny-shaped cracks comprises an elastic opening

v_E and a creep opening v_C. Use of the reciprocal theorem and Eq. (8) gives

$$\frac{v_E}{\bar{R}} = \frac{3}{\pi f}\frac{1-\chi}{\chi}\frac{(\sigma_h^\infty - T)}{E_0} \tag{9}$$

Compatibility dictates that the total displacement $v = v_E + v_C$ equals the sum of the extra displacement due to the spring-like extension of asperities u_S, the plating of matter by sintering at the contacting asperities $w - w_1$ and an initial asperity height u_1 due to wedging of one asperity against its neighbour on the opposing face, such that

$$v = v_E + v_C = u_S + w - w_1 + u_1 \tag{10}$$

The contact stiffness k of the asperities is defined by

$$T = ku_S \tag{11}$$

and has an explicit nonlinear dependence upon b/s, see Fleck and Cocks [5].

The bridging traction T depends upon the imposed hydrostatic stress σ_h^∞ and upon the asperity geometry according to

$$\frac{T}{E_1} = \left(\frac{\bar{R}k}{\bar{R}k + E_1}\right)\left(\frac{\sigma_h^\infty}{E_1} + \frac{v_C + w_1 - u_1 - w}{\bar{R}}\right) \tag{12}$$

where

$$E_1 \equiv \frac{\pi}{3}\frac{\chi f}{1-\chi}E_0 \tag{13}$$

The elastic strain energy density of the cracked solid, including the contribution from elastic indentation of each asperity, is

$$U = \frac{1}{2}\sigma_{ij}^\infty \varepsilon_{Eij} + \frac{\pi}{2} fT\frac{(u_S - v_E)}{\bar{R}} \tag{14}$$

5.3. Creep response

We assume that the splats undergo Coble creep, such that the macroscopic creep rate is linear in remote stress. Consider the creep response of the micro-cracked solid shown in Fig. 1: the matrix creeps in an incompressible manner with a shear viscosity η_0, in addition to its linear elastic response. The creep rate $\dot{\varepsilon}_{Cij}$ is related to the macroscopic mean stress σ_h^∞ and deviatoric stress $s_{ij}^\infty \equiv \sigma_{ij}^\infty - \sigma_h^\infty \delta_{ij}$ via the isotropic relation,

$$\dot{\varepsilon}_{Cij} = \frac{(2+\chi)}{6\chi\eta_0}s_{ij}^\infty + \frac{1}{3}\left(\frac{1-\chi}{\chi}\right)\frac{(\sigma_h^\infty - T)}{\eta_0}\delta_{ij} \tag{15}$$

Further, the rate of crack opening $\dot{v}_C$ due to creep can be related directly to the volumetric creep rate $\dot{\varepsilon}_{Ch}$, giving

$$\dot{v}_C = \frac{\bar{R}\dot{\varepsilon}_{Ch}}{\pi f} = \left(\frac{1-\chi}{\chi}\right)\frac{\bar{R}}{\pi f}\left(\frac{\sigma_h^\infty - T}{\eta_0}\right) \tag{16}$$

5.4. The dissipation potential due to local sintering and Coble creep

It is assumed that matter diffuses along the interface from the contacts in Fig. 2c, and deposits along the free surfaces of length ℓ. Matter diffuses from the sides of asperities, of local surface energy γ_S to contacts with interfacial energy γ_G .

Introduce the rate potential Ψ_S for a representative single asperity. The potential Ψ_S is expressed in terms of the volumetric interfacial flux j; this flux is labelled j_1 and is a function of the arc length s_1 along the contact OA of Fig. 2c. Likewise, it is labelled j_2 and is a function of the arc length s_2 along the contact AB, as shown in Fig. 2c. Define

$$\Psi_S = \frac{1}{D_G}\int_0^b \pi s_1 j_1^2 ds_1 + \frac{\cos\beta}{D_S}\int_{b/\cos\beta}^{\ell+(b/\cos\beta)} \pi s_2 j_2^2 ds_2 \tag{17}$$

where (D_G, D_S) are the diffusion constants for interfacial diffusion along OA and surface diffusion along the free surface AB, respectively. The flux $j_1(s_1)$ along OA is related directly to the rate of separation $\dot{w}$ of two contacting columns according to

$$j_1 = -\frac{1}{2}\dot{w}s_1 \tag{18}$$

on OA. Similarly, the flux $j_2(s_2)$ along AB is given by

$$j_2 = \left(\frac{A_1}{s_2} + B_1 s_2 + C_1 s_2^2\right)\dot{w} + \left(\frac{A_2}{s_2} + B_2 s_2 + C_2 s_2^2\right)\dot{\lambda} \tag{19}$$

with explicit expressions for (A_i, B_i, C_i) listed in Appendix A of Fleck and Cocks [5].

Ψ_S is a quadratic function of $(\dot{w}, \dot{\lambda})$ and is obtained by integration of Eq. (17); it also depends upon the current state (w, λ). The total dissipation per unit volume Ψ within the solid from sintering and bulk creep follows as

$$\Psi = \frac{4f}{\bar{R}s^2}\Psi_S + \frac{1}{2}\sigma_{ij}^\infty \dot{\varepsilon}_{Cij} - \frac{\pi}{2} fT\frac{\dot{v}_C}{\bar{R}} \tag{20}$$

5.5. The free energy and the variational statement

The free surface energy per asperity reads

$$G_S = \pi b^2(\gamma_G - \gamma_S) + \frac{\pi}{4}\frac{1}{\cos\beta}(\lambda^2 - 4b^2)\gamma_S - \frac{\pi}{4}\lambda^2\gamma_S \tag{21}$$

and the total Gibbs free energy per unit volume G is

$$G = U + \frac{4f}{\bar{R}s^2}G_S - \sigma_{ij}^\infty \varepsilon_{ij} \tag{22}$$

where the internal strain energy U has already been stated by Eq. (14). We emphasize that G depends upon the primary variables $(w, \lambda, \sigma_{ij}^\infty, T)$.

The rate quantities $(\dot{w}, \dot{\lambda})$ are determined by minimizing the functional $\Omega(\dot{w}, \dot{\lambda}) \equiv \dot{G} + \Psi$, where $\dot{G}$ is obtained by differentiating Eq. (22) with respect to time, and is linear in $(\dot{w}, \dot{\lambda})$. The minimization process gives

$$\begin{pmatrix} \frac{\partial^2\Psi}{\partial\dot{w}^2} & \frac{\partial^2\Psi}{\partial\dot{w}\partial\dot{\lambda}} \\ \frac{\partial^2\Psi}{\partial\dot{w}\partial\dot{\lambda}} & \frac{\partial^2\Psi}{\partial\dot{\lambda}^2} \end{pmatrix}\begin{pmatrix}\dot{w}\\ \dot{\lambda}\end{pmatrix} = -\begin{pmatrix}\frac{\partial\dot{G}}{\partial\dot{w}}\\ \frac{\partial\dot{G}}{\partial\dot{\lambda}}\end{pmatrix} \tag{23}$$

This can be inverted algebraically to obtain $(\dot{w}, \dot{\lambda})$ as a function of the current state (w, λ, v_C). The time evolution

of (w, λ) follows by integration using any convenient scheme.

The set of constitutive relations are now complete. At any given state, the macroscopic elastic strain is specified by Eq. (8), in terms of the bridging traction T as given by Eq. (12). The macroscopic creep strain rate and the rate of crack opening due to creep deformation are obtained from Eqs. (15) and (16), respectively, while the contact geometry evolves according to Eq. (23).

The constrained sintering response is explored in the following section. In many cases, the asperities quickly evolve to the shape of a circular cylinder, with $\beta \to \pi/2$. After this shape has been attained, w and λ are no longer independent state variables but are directly related by conservation of volume of an asperity. $\dot{\lambda}$ follows directly from $\dot{w}$ and the system of two equations (23) reduces to a single rate equation for $\dot{w}$:

$$\frac{d^2\Psi}{d\dot{w}^2}\dot{w} = -\frac{d\dot{G}}{d\dot{w}} \tag{24}$$

The details are given in Appendix A.

6. The constrained sintering problem

We consider the practical problem of an APS layer, of thermal expansion coefficient α_{TBC} upon a thick substrate of nickel-rich superalloy, of thermal expansion coefficient α_S. The substrate is taken to be stress-free and at a uniform temperature Θ_S. The coating is thin in the through-thickness, x_3 direction, compared with the in-plane (x_1, x_2) directions.

The coating is deposited at a temperature Θ_D, and during operation the temperature within the coating Θ can vary with depth. Then, the thermal strain ε_T at any depth within the coating is given by Eq. (1). Now use Greek subscripts to denote the in-plane (x_1, x_2) directions. Then, the thermal strain ε_T is accommodated by elastic strain $\varepsilon_{E\alpha\beta} = \varepsilon_E\delta_{\alpha\beta}$ and creep strain $\varepsilon_{C\alpha\beta} = \varepsilon_C\delta_{\alpha\beta}$ within the coating, such that

$$\varepsilon_T + \varepsilon_E + \varepsilon_C = 0 \tag{25}$$

The coating acquires an equi-biaxial state of stress $\sigma_{11} = \sigma_{22} = \sigma$, $\sigma_{33} = 0$. The elastic constitutive law (8) for the *TBC* reduces to:

$$\varepsilon_E = \left(\frac{1-\nu}{E}\right)\sigma - \left(\frac{1-\chi}{\chi}\right)\frac{T}{E_0} = -(\varepsilon_T + \varepsilon_C) \tag{26}$$

where

$$\frac{T}{E_1} = \left(\frac{\bar{R}k}{\bar{R}k + E_1}\right)\left(\frac{2}{3}\frac{\sigma}{E_1} + \frac{v_C - w + w_1 - u_1}{\bar{R}}\right) \tag{27}$$

via Eq. (11). The salient creep rates are

$$\frac{\pi f}{\bar{R}}\dot{v}_C = \left(\frac{1-\chi}{\chi}\right)\left(\frac{2\sigma - 3T}{3\eta_0}\right) \tag{28}$$

and

$$\dot{\varepsilon}_C = \frac{2+\chi}{18\chi\eta_0}\sigma + \frac{\pi f}{3\bar{R}}\dot{v}_C \tag{29}$$

via Eqs. (15) and (16). In the current state, $(\varepsilon_T, v_C, \varepsilon_C)$ are known and so (σ, T) are obtained by solving the two simultaneous Eqs. (26) and (27). The rates $(\dot{v}_C, \dot{\varepsilon}_C)$ are specified by Eqs. (28) and (29). Additionally, Eq. (23) gives $(\dot{w}, \dot{\lambda})$. A fourth-order Runge–Kutta procedure is used to integrate $(\dot{w}, \dot{\lambda}, \dot{v}_C, \dot{\varepsilon}_C)$ forward in time, with $(w, \lambda, v_C, \varepsilon_C)$ known in the current state.

6.1. Constrained sintering response

Consider the problem of heating the APS ceramic layer and substrate to a sufficiently high temperature (say 1000 °C) that the ceramic undergoes bulk creep and sintering of the penny-shaped cracks. In general, the coating has a temperature gradient across it, and the mismatch in thermal expansion properties between coating and substrate gives rise to a thermal mismatch strain $\varepsilon_T(x_3)$ where x_3 is the through-thickness direction.

Consider first the general problem of a *TBC* layer with a prescribed temperature jump between the top and bottom of the coating. As the coating sinters, its thermal conductivity and Young's modulus increase with time, and consequently the temperature profile $\Theta(x_3)$ changes. The kinetic constants for diffusion and bulk creep vary exponentially with temperature in an Arrhenius manner, and so the subsequent sintering rate will vary nonlinearly with position x_3, and in turn this leads to a non-uniform temperature profile. Whilst calculations of this type can be performed without difficulty, adequate physical insight into constrained sintering is obtained by assuming that the temperature Θ at any given location x_3 is held constant. In the ensuing analysis, ε_T is held fixed and the transient sintering response is determined along with the change in macroscopic modulus of the coating.

6.1.1. The initial state

The initial value of radius b of the asperities is determined by the initial value of compressive traction $|T|$ bridging the cracks. Assume that the indentation pressure at each asperity is $3\sigma_Y$. Then, equilibrium dictates that the initial radius is

$$b = b_1 = \frac{s}{2}\left(\frac{|T|}{3\sigma_Y}\right)^{1/2} \tag{30}$$

The initial height of asperity $w(t=0) \equiv w_1$ follows immediately from Eq. (2) as

$$w_1 = w_0\lambda_0^2\left[\frac{3}{4}\lambda_0^2 + \left(2b_1 + \frac{\lambda_0}{2}\right)^2\right]^{-1} \tag{31}$$

It remains to obtain the initial asperity height u_1 associated with asperity wedging. Substitution of Eqs. (9) and (11) into the compatibility statement (Eq. (10)) gives

$$u_1 = v_E - u_S = \frac{\bar{R}}{\pi f}\left(\frac{1-\chi}{\chi}\right)\left(\frac{2\sigma - 3T}{E_0}\right) - \frac{T}{k} \tag{32}$$

where σ is given by Eq. (26), with $\varepsilon_C = 0$.

6.1.2. Evolution of bulk modulus during sintering

It is assumed that the contacting asperities have a normal contact stiffness but a vanishing shear stiffness; this is consistent with the notion that free sliding can occur at interfaces such as grain boundaries at elevated temperature. Consequently, sintering leads to an increase in the contact stiffness k and thereby to a progressive increase in macroscopic bulk modulus, but not shear modulus at elevated temperature. The effective bulk modulus K_{eff} is given by

$$\frac{1}{K_{eff}} \equiv \frac{d\varepsilon_{Eh}}{d\sigma_h^{\infty}} = \frac{1}{K} - \frac{3(1-\chi)}{\chi E_0} \frac{\bar{R}k}{E_1 + \bar{R}k} \tag{33}$$

as discussed by Fleck and Cocks (2009). Here, K is the bulk modulus for the micro-cracked solid containing traction-free penny-shaped cracks as specified by Eq. (6); E_1 has already been defined in Eq. (13).

6.1.3. Characteristic timescales

It proves convenient to evaluate the computational results in terms of three characteristic timescales. Fleck and Cocks [5] identified the dominant timescales for the HIP problem, based on the application of a constant pressure which is much greater than the sintering stress. Under constrained sintering, the stresses generated in the coating scale with the sintering stress, and the sintering stress evolves with the geometry of the asperities. Suitable characteristic timescales are determined below.

(i) In the current problem, the equi-biaxial stress within the coating evolves from its initial value, as set by (T, ε_T), to a level on the order of the sintering stress (as given by Eq. (35) below) over a timescale of $\tau_1 \equiv \eta_0/E_0$. This time constant gives the period for creep relaxation of the uncracked solid in the absence of diffusion at the asperities. Typically, τ_1 is much less than the time constant for creep relaxation by local diffusion at the asperity level. Elasticity plays a minor role over timescales exceeding τ_1.

Two additional timescales τ_2 and τ_3 emerge, by the following arguments. It is shown below in the results section that the timescale for constrained sintering is comparable to that for free sintering. Accordingly, we can estimate the timescale for constrained sintering by considering the simpler problem of free sintering, with $\sigma \equiv 0$. Also, the sintering rate for circular cylindrical asperities is comparable to that for a conical frustum. Consequently, a simple analytical model is developed in Appendix B, based upon the notion that sintering of cylindrical asperities is driven by the sintering stress σ_S, which arises from the reduction of interfacial energy of the contacting asperities with respect to asperity height w. As the asperities grow λ becomes much larger than w, and Eq. (A2) simplifies to

$$G_S = \frac{\pi}{4}\lambda^2(\gamma_G - 2\gamma_S) \tag{34}$$

The sintering stress at the scale of the cracks follows immediately as

$$\sigma_S \equiv \frac{4}{\pi s^2}\frac{\partial \dot{G}_S}{\partial \dot{w}} = \frac{(2\gamma_S - \gamma_G)}{w}\left(\frac{\lambda}{s}\right)^2 \tag{35}$$

upon making use of the volumetric constraint (A1) between λ and w.

Asperity sintering necessarily involves accommodation by creep deformation as stipulated by Eq. (10). Two timescales emerge, depending upon whether local diffusion or bulk creep is the dominant dissipative process. Both processes are driven by the sintering stress, with the details given in Appendix B. Here, we state only the results.

(ii) When the creep viscosity is high, sintering is constrained and the magnitude of the traction T approaches the sintering stress σ_S. The characteristic time for closure of the penny-shaped cracks by Coble creep is obtained by equating T in Eq. (16) to σ_S and setting $\sigma_h^{\infty} = 0$. Integration of the resulting expression from an initial asperity height w_1 as defined by Eq. (31) gives the time to close the cracks by creep:

$$\tau_2 = \frac{\pi f \chi}{(1-\chi)}\frac{\eta_0}{(2\gamma_S - \gamma_G)}\frac{s^2 w_1^3}{\bar{R}\lambda_0^2 w_0} \tag{36}$$

(iii) When the creep viscosity is small, sintering of the asperities is readily accommodated and the traction T across the faces of the crack is zero. Sintering of the asperities is again driven by the sintering stress, which arises from the reduction of total interfacial energy of the contacting asperities. The analysis in Appendix B provides a characteristic timescale of

$$\tau_3 = \frac{\lambda_0^2 w_0 w_1}{96 D_G(2\gamma_S - \gamma_G)} \tag{37}$$

6.1.4. Typical response

In order to allow for immediate comparison between the free sintering response and the HIP response, we assume the same geometry as that considered by Fleck and Cocks [5]: $\bar{R} = 100\ \mu m$, $s = 5\ \mu m$, $\lambda_0 = 1\ \mu m$, $w_0 = 0.5\ \mu m$ and $f = 0.43$. Likewise, the pertinent material properties at 1300 °C are given by $E_0 = 170$ GPa, $\sigma_Y = 400$ MPa, $\eta_0 = 800$ GPa s, $D_S = D_G = 6.3 \times 10^{-31}\ m^6\ J^{-1}\ s^{-1}$, $\gamma_S = 1\ J\ m^{-2}$ and $\gamma_G = 0.64\ J\ m^{-2}$. The value of $f = 0.43$ has been chosen in order to give an initial value for the Young's modulus of the APS material of 40 GPa, as typically observed. The initial compressive traction across the cracks is taken to be $T = -5$ MPa, and the thermal expansion mismatch is taken to be $\varepsilon_T = 0$. The resulting values of the time constants are $\tau_1 = 4.71$ s, $\tau_2 = 5.27 \times 10^3$ s and $\tau_3 = 2.13 \times 10^3$ s.

We note in passing that $\tau_1/\tau_2 = 8.94 \times 10^{-4}$, with the interpretation that rapid creep relaxation of stress occurs early in the life of the coating. As already discussed by Fleck and Cocks [5], τ_1/τ_2 gives a measure of the ratio of elastic opening of the penny-shaped cracks to the asperity

height. Thus, asperity sintering cannot be accommodated by elastic closure of the cracks alone, but requires Coble creep.

The geometric constraint (Eq. (10)) implies that the diffusional flattening of asperities w is accommodated by creep closure of the penny-shaped cracks v_C. Consequently, the sintering time is governed by the longer of the times τ_2 and τ_3. Upon adopting the above numerical values for geometric and material properties we obtain $\tau_3/\tau_2 = 0.404$ and conclude that, for this choice, the overall sintering time is dictated by both Coble creep and diffusional flattening of the matrix. We explore the role of τ_3/τ_2 further below.

7. Results

We begin by showing the evolution of stress state and contact size within the coating, for values of ε_T in the practical range of -0.2% to 0.2%, see Fig. 3. Time t is normalized by τ_1 in order to emphasize that (T, σ) decay by Coble creep over a period on the order of τ_1 from their initial values to a level on the order of the sintering stress, which scales with $(2\gamma_S - \gamma_G)/\lambda_0$. During this initial transient, the contact size b is almost constant. Significant sintering occurs after a much longer time period, on the order of τ_2 or τ_3, as described in Section 7.1 below. It is clear from Fig. 3 that the value of ε_T dictates the initial value of in-plane stress σ but has almost no effect upon the evolution of crack traction T and upon contact size b. The rapid relaxation of in-plane stress by Coble creep has already been demonstrated in Fig. 5 of Ref. [10]: the stress drops to almost zero over 10 h at 1400 °C.

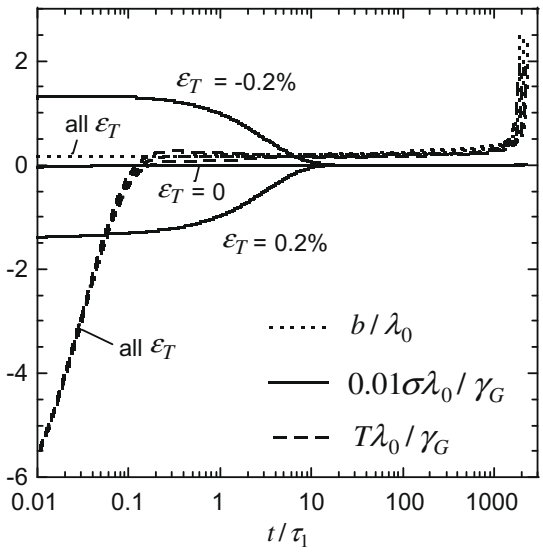

Fig. 3. Evolution with time of the in-plane stress σ in the coating, contact radius of asperity b and the traction T across the faces of each penny-shaped crack due to asperity bridging. Predictions are given for selected values of the linear thermal expansion mismatch strain ε_T, for the choice of geometric and material parameters as listed in Section 6.1. The time constants (τ_1, τ_2, τ_3) are held fixed.

7.1. The role of relative timescales

The effect of timescales (τ_2, τ_3) upon the sintering response is explored in Fig. 4 for $\varepsilon_T = 0$. Specifically, with $\tau_3 = 2.13 \times 10^3$ s, τ_2, has the selected values of 5.27×10^1 s, 5.27×10^3 s and 5.27×10^5 s by suitable selection of values for η_0. When τ_3/τ_2 is less than about unity, the sintering rate is dictated by the characteristic time τ_2 for crack closure by Coble creep. In contrast, when τ_3/τ_2 is greater than about unity, the sintering rate is controlled by the characteristic time τ_3 for diffusional flow at asperi-

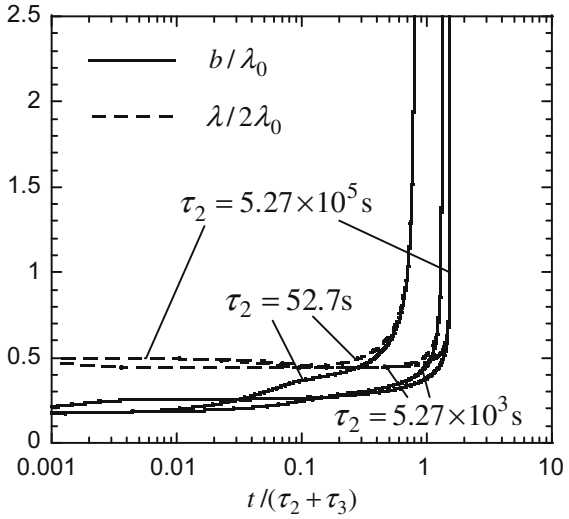

Fig. 4. Evolution of contact radius of asperity top b and the diameter of the asperity base λ with time, for selected values of τ_2 with τ_3 held fixed. τ_2 (and τ_1) are varied by selecting values for the viscosity η_0. The thermal expansion mismatch strain ε_T equals zero, and the values for the geometric and material parameters are listed in Section 6.1.

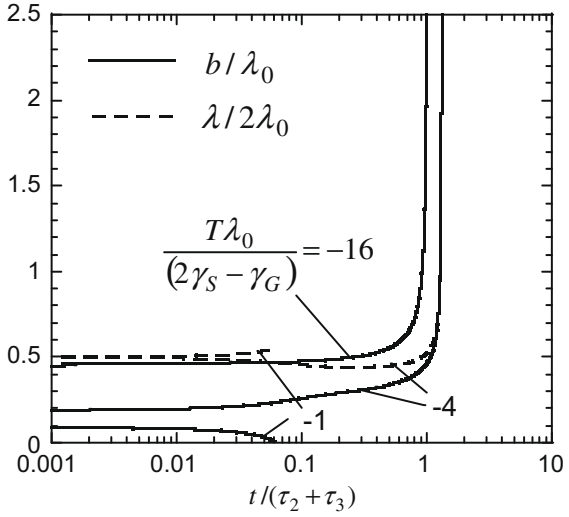

Fig. 5. Evolution of contact radius of asperity top b and the diameter of the asperity base λ with time, for selected values of initial traction T. The time constants (τ_1, τ_2, τ_3) are held fixed. The thermal expansion mismatch strain ε_T equals zero, and the values for the geometric and material parameters are listed in Section 6.1.

ties. Accordingly, time has been normalized by $\tau_2+\tau_3$ in Fig. 4. The normalized sintering response lies in a narrow band, with complete sintering of the asperities occurring at $t/(\tau_2+\tau_3)\approx 1$, despite the fact that η_0 ranges by four orders of magnitude.

7.2. The sensitivity of sintering time to initial contact size

The initial contact size b_1 is dictated by the choice of initial traction T. The constrained sintering response is shown in Fig. 5 for selected values of compressive traction, with $\varepsilon_T=0$. The choice of normalization for time is able to capture the sensitivity of sintering response to initial contact size, except for the case of small b_1 (associated with $T\lambda_0/(2\gamma_S-\gamma_G)=-1$). In this case, b decreases with increasing time and desintering occurs. An examination of the response for $T\lambda_0/(2\gamma_S-\gamma_G)=-1$ reveals that the crack opening v_c and asperity height w remain constant with increasing time, and so additional insight into the desintering phenomenon can be gleaned by plotting the free energy per asperity G_S as a function of b, for fixed values of $w=w_1$, see Fig. 6. The initial geometry (b_1, w_1) is dictated by the initial traction $|T|$: the circles marked on each curve in Fig. 6 are the initial geometries for each of the three values of $|T|$ considered in Fig. 5. For the two larger initial values of $|T|$ the free energy decreases with increasing contact radius b of the asperity, and sintering proceeds with increasing time. The decrease in free energy drives material rearrangement by surface diffusion so that the shape of the asperity evolves towards the minimum in the free energy profile. In contrast, for $T\lambda_0/(2\gamma_S-\gamma_G)=-1$, the free energy decreases with diminishing b and this drives desintering. The desintering phenomenon is sensitive to the initial geometry of the asperity: more detailed descriptions of the shape of the asperities are required to fully capture the behaviour when the contacts are small.

If the constraint of the matrix is reduced by a large degree, for example, by significantly reducing the creep viscosity η_0, the asperity can evolve towards a lower energy configuration by reducing its height w in addition to changing its contact size b. For the choice $T\lambda_0/(2\gamma_S-\gamma_G)=-1$, the asperities can now sinter and sintering is complete when $t\approx(\tau_2+\tau_3)$, as before. This alternative response is not shown explicitly here, but was deduced by numerical experimentation.

The desintering phenomenon described above is similar to the morphological instabilities observed in constrained polycrystalline fibres by Miller and Lange [17] and modelled by Sun et al. [18]. Polycrystalline fibres, when constrained in a matrix which prevents shrinkage, can break up into isolated spherical grains if the ratio of the grain size to fibre diameter exceeds a critical value.

7.3. Effect of asperity spacing

We have demonstrated above that the overall timescale for the sintering process is determined by the larger of τ_2 and τ_3. The detailed response, including the evolution of elastic modulus, depends upon the choice of internal geometric parameters. Fig. 7 shows the effect of varying the asperity spacing s upon the evolution of the bulk modulus, which is normalized by the modulus of the fully dense material K_0. In these simulations, we take $\bar{R}=50$ μm and $f=0.5$, and s is varied between 5 μm and 20 μm. The value of initial crack face traction T is chosen to provide the same initial geometry of asperities, i.e. $b_1=0.144$ μm and $w_1=0.364$ μm, for each simulation. All other geometric and kinetic parameters are the same as those for the reference case of Fig. 3. The characteristic timescales $\tau_1=4.7$ s and $\tau_3=2.22\times10^3$ s are fixed for all simulations, but τ_2, which is proportional to s^2, varies from 5.59×10^3 s for $s=5$ μm to 8.94×10^4 s for $s=20$ μm,

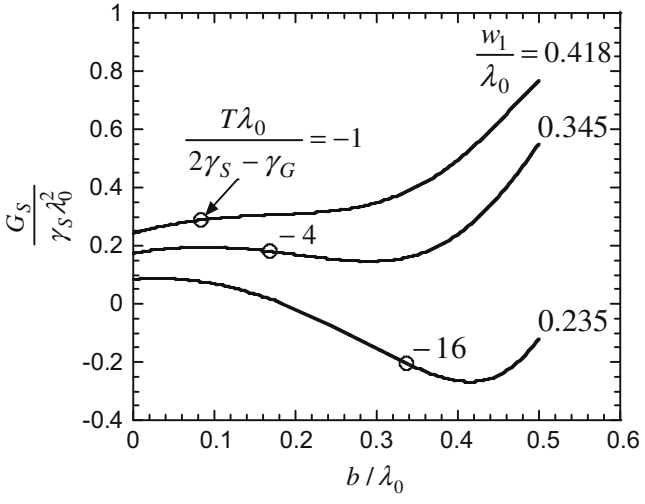

Fig. 6. Sections through the energy landscape for a single asperity for different values of asperity height w. The initial free energy and values of asperity height w_1 and contact radius b_1 corresponding to three different values of initial crack face traction T are indicated by circles.

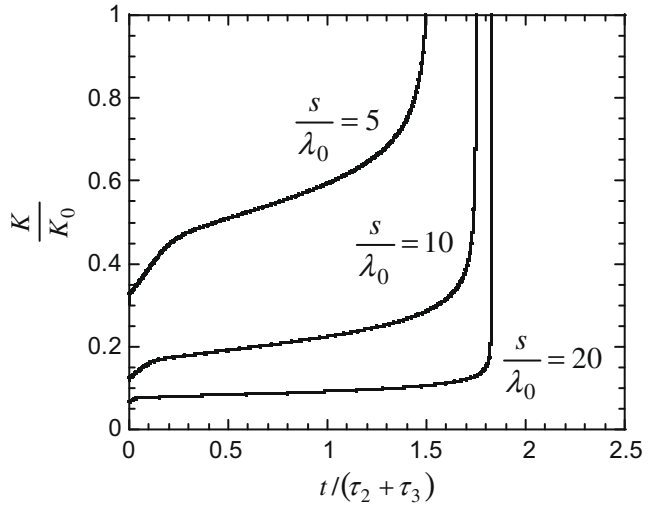

Fig. 7. The effect of asperity spacing s upon the evolution of bulk modulus.

recall Eq. (36). In all cases, sintering is complete when $t \approx (\tau_2 + \tau_3)$, but the detailed response is sensitive to the choice of s. The closer the spacing of the asperities, the higher the initial modulus. For small values of s, there is a gradual increase in modulus towards full density, while for large asperity spacing the modulus increases rapidly initially and then remains almost constant until $t \approx (\tau_2 + \tau_3)$, when it increases rapidly once more towards full density. This latter response is consistent with the experimental observations described in the introduction [2,4,7]. For example, Choi et al. [2] observed an increase in modulus by a factor of two, followed by a plateau in response. However, the experiments which have been reported in the literature to date are of short duration and do not detect the final rise in stiffness due to full sintering.

7.4. Comparison of constrained and free sintering

The time evolution of contact geometry and of bulk modulus $(w/\lambda_0, b/\lambda_0, \lambda/\lambda_0, v_c/\lambda_0, K/K_0)$ is plotted in Fig. 8 for both free sintering and constrained sintering (with $\varepsilon_T = 0$) using the reference set of parameters as given at the end of Section 6. The two responses are qualitatively the same, except for the feature that imposition of substrate constraint doubles the sintering time. This factor depends on the detailed internal geometry and the relative rates of asperity sintering and Coble creep; it typically ranges from about 1.5 to 2.5. This suggests that free sintering experiments can be used to mimic constrained sintering, with suitable allowance for a shift in timescale, provided the internal geometric parameters are the same in each case.

When $\varepsilon_T > 0$, such as near the free surface of a coating in-service, an in-plane compressive stress is generated initially in the coating, and this compressive stress partially closes the cracks. As a result, the magnitude of the traction across the faces of the intersplat cracks increases. This will result in a plastic flattening of the asperities and to an increase in modulus. Conversely, when $\varepsilon_T < 0$, such as in the constrained coating adjacent to the substrate in-service or in isothermal experiments, such as those conducted by Thompson and Clyne [4], the intersplat cracks will tend to open as the temperature is increased, resulting in the breaking apart of some asperity contacts and leading to an increase in the mean asperity spacing, s, compared with that for the virgin material. This will result in a decrease in initial modulus and a slower rate of increase of modulus by sintering, as discussed in Section 7.3. This behaviour is consistent with the experimental observations of Thompson and Clyne [4], who measured smaller values of initial modulus and a smaller increase in modulus before plateaus were attained in the constrained coating compared with the free sintering case. More detailed experimental studies are required to provide information about asperity spacing and how this is influenced by the transient temperature history to the hold condition, before a full quantitative assessment can be made of the available experimental data.

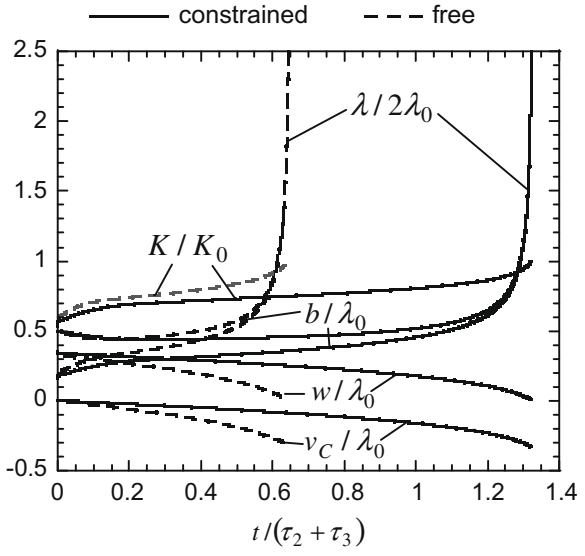

Fig. 8. Evolution with time of the contact geometry (as given in terms of dimensionless b, λ, w, and v_C) and of the dimensionless bulk modulus K. The constrained and free sintering cases are both shown for comparison. The thermal expansion mismatch strain ε_T equals zero, and the values for the geometric and material parameters are listed in Section 6.1.

Cipitria et al. [10] have measured and predicted the evolution of TBC coating thickness for both constrained and free sintering. The experimental data show that the strain increases to a value of about 1% over a time of 20 h. This is due to closure of the intersplat cracks and is sensitive to the initial asperity size and splat thickness. Their calculations and experiments both indicate that the rate of thinning in a constrained layer is about 30% faster than that in an unconstrained, free-standing layer. It is instructive to compare the predictions of the current model with their results.

The present analysis of constrained sintering assumes that the change in coating thickness due to asperity sintering and Coble creep is directly related to the creep component of crack opening v_C. Write h as the initial coating thickness and Δh as the decrease in coating thickness. Then, Eq. (16) gives

$$\frac{\Delta h}{h} = \left(\frac{\pi f \lambda_0}{\bar{R}}\right) \frac{v_C}{\lambda_0} \tag{38}$$

and it is clear that the change in coating thickness due to creep is kinematically linked to the degree of asperity sintering. The above relation is modified to

$$\frac{\Delta h}{h} = \frac{1}{3}\left(\frac{\pi f \lambda_0}{\bar{R}}\right) \frac{v_C}{\lambda_0} \tag{39}$$

for an unconstrained layer. However, the rate of crack closure $\dot{v}_C$ for unconstrained sintering is between 1.5 and 2.5 times that for constrained sintering, as discussed above. Consequently, the current model predicts that the rate of thickness reduction for constrained sintering is between 20% and 100% faster than that for unconstrained sintering; this ratio depends somewhat upon the concentration of penny-shaped cracks, and upon the relative rate of asperity

sintering to bulk creep. It is concluded that the present model gives similar trends to the experiments and predictions of Cipitria et al. [10]. In addition, the present treatment gives insight into the cross-coupling between sintering rate and the evolution of modulus of the coating, as already noted above.

8. Concluding remarks

A multi-scale model has been developed for the constrained sintering of an APS thermal barrier coating. Three characteristic timescales emerge: τ_1 for stress relaxation by Coble creep, τ_2 for crack closure by Coble creep, and τ_3 for asperity sintering by local diffusion. In practice τ_1 is the smallest, and the sintering time is dictated by the larger of τ_2 and τ_3. The model successfully predicts that the modulus of the coating can double or more during the early stages of sintering and then remain almost constant for a long period. Additional experiments are required before a quantitative comparison can be made between the predicted evolution of microstructure (and modulus) and that observed in practice.

The current model is based upon the Budiansky–O'Connel treatment of an isotropic distribution of penny-shaped cracks. It is appreciated that the out-of-plane modulus of the as-deposited coating is 30–40% greater than the in-plane modulus, see for example Refs. [16] and [19]. However, as sintering proceeds the difference diminishes. For example, the ratio of moduli in the two directions diminishes from 30% to 5% over a sintering time of 200 h at 1150 °C, see Ref. [19]. Thus the assumption of isotropy improves with the progression of sintering. When making comparisons between the model and measurement, the in-plane modulus is considered in the above treatment. We emphasize that we assume isotropy for the sake of simplicity and to highlight the main physics of sintering of these materials.

Acknowledgements

The authors are grateful for financial support from the US Office of Naval Research (Grant No. N00014-05-1-0376, contract monitor Dr David Shifler) and to the EPSRC (Grant No. EP/C52392X/01). Technical discussions with Drs Stefan Lampenscherf and Alessandro Casu of Siemens AG are much appreciated.

Appendix A: The circular cylindrical asperity

After the inclination β of each asperity has attained the value of $\pi/2$, the contact evolves with $2b \equiv \lambda$. Within this regime of behaviour, the evolution of asperity size is governed by the single degree of freedom w instead of (w, λ). Consider a circular, cylindrical asperity of height w and diameter λ. Volume conservation dictates that

$$\lambda = \lambda_0 \left(\frac{w_0}{3w}\right)^{1/2} \tag{A1}$$

in terms of the reference configuration as defined in Fig. 3a. The total Gibbs free energy per unit volume G is still given by Eq. (22) but the expression for the free surface energy per asperity (21) is modified to

$$G_S = \frac{\pi}{4}\lambda^2(\gamma_G - 2\gamma_S) + \pi\lambda w\gamma_S \tag{A2}$$

Likewise, the total dissipation per unit volume Ψ remains that stated in Eq. (20), whereas the potential Ψ_S for each asperity simplifies to

$$\Psi_S = \left[\frac{\pi}{256}\frac{\lambda^4}{D_G} + \frac{\pi}{96}\frac{w\lambda^3}{D_S}\right]\dot{w}^2 \tag{A3}$$

The rate quantity $\dot{w}$ is obtained by minimizing the functional $\Omega(\dot{w}) \equiv \dot{G} + \Psi$, where $\dot{G}$ is obtained by differentiating Eq. (22) with respect to time, and is linear in $\dot{w}$. The minimization results in the single algebraic equation

$$\dot{w} = -\left(\frac{d^2\Psi}{d\dot{w}^2}\right)^{-1}\frac{d\dot{G}}{d\dot{w}} \tag{A4}$$

instead of Eq. (23).

Appendix B: Characteristic times for sintering

In this appendix we derive simple equations for sintering of the asperities in the limits where either diffusion at the scale of the asperities or Coble creep of the matrix controls the sintering rate. We idealize the asperities as cylinders and make use of the equations developed in Appendix A.

B.1. Characteristic time for accommodation by creep of the surrounding matrix

Consider the limit where the creep viscosity η_0 is large. A traction $T \approx \sigma_S$ is generated across the faces of the cracks, with σ_S given by Eq. (35). The crack opening rate is given by Eq. (28), and for zero applied stress this simplifies to

$$\begin{aligned}\dot{v}_c = \dot{w} &= -\frac{(1-\chi)\bar{R}}{\pi f\chi\eta_0}T \\ &= -\frac{(1-\chi)\bar{R}}{\pi f\chi\eta_0}\frac{(2\gamma_S - \gamma_G)}{w}\left(\frac{\lambda}{s}\right)^2\end{aligned} \tag{B1}$$

The characteristic time for sintering by diffusion at the asperity scale τ_2 is obtained by integrating Eq. (B1) between the limits $w = w_1$ at $t = 0$ and $w = w_f \approx 0$ at $t = \tau_2$, with due regard to the constraint (A1), giving

$$\tau_2 = \frac{\pi f\chi}{(1-\chi)}\frac{\eta_0}{(2\gamma_S - \gamma_G)}\frac{s^2 w_1^3}{\bar{R}\lambda_0^2 w_0} \tag{B2}$$

Recall that (λ_0, w_0) specifies the reference configuration, with w_1 given by Eq. (31).

B.2. Sintering controlled by diffusion at the scale of the asperities

Alternatively, consider the limit where the creep viscosity η_0 is small, so that diffusion at the scale of the asperities is readily accommodated by creep of the surrounding matrix. Then, the dissipation of energy by creep is much less than that due to local diffusion. As the asperities grow λ becomes much larger than w. Also, in general $D_S \geqslant D_G$. Making use of Eq. (A4) we can then write

$$\Psi = \frac{4\Psi_S}{\pi s^2} \approx \left[\frac{1}{64}\frac{\lambda^4}{s^2 D_G}\right]\dot{w}^2 \tag{B3}$$

Eq. (A4) then gives, after noting Eq. (34),

$$\dot{w} = \frac{32(\gamma_G - 2\gamma_S)D_G}{\lambda^2 w} = \frac{96(\gamma_G - 2\gamma_S)D_G}{\lambda_0^2 w_0} \tag{B4}$$

The characteristic time for sintering by diffusion at the asperity scale τ_3 is obtained by integrating Eq. (B4) between the limits $w = w_1$ at $t = 0$ and $w = w_f \approx 0$ at $t = \tau_3$, giving

$$\tau_3 = \frac{\lambda_0^2 w_0 w_1}{96 D_G(2\gamma_S - \gamma_G)} \tag{B5}$$

References

[1] Zhu D, Miller RA. Surf Coat Technol 1998;108–109:114.
[2] Choi SR, Zhu D, Miller RA. J Am Ceram Soc 2005;88:2859.
[3] Cernuschi F, Bison PG, Marinetti S, Scardi P. Acta Mater 2008;56:4477.
[4] Thompson JA, Clyne TW. Acta Mater 2001;49:1565.
[5] Fleck NA, Cocks ACF. J Mech Phys Solids 2009;57:689.
[6] Wakui T, Malzbender J, Steinbrech RW. Surf Coat Technol 2006;200:4995.
[7] Lampenscherf S. Private communication.
[8] Soltani R, Coyle TW, Mostaghimi J. J Spray Technol 2008;17:244.
[9] Cipitria A, Golosnoy IO, Clyne TW. Acta Mater 2009;57:980.
[10] Cipitria A, Golosnoy IO, Clyne TW. Acta Mater 2009;57:993.
[11] Bordia R, Jagota A. J Am Ceram Soc 1993;76:2475.
[12] Guillon O, Aulbach E, Rödel J, Bordia R. J Am Ceram Soc 2007;90:1733.
[13] Hutchinson RG, Fleck NA, Cocks ACF. Acta Mater 2006;54:1297.
[14] Cocks ACF, Gill SPA, Pan J. Adv Appl Mech 1999;36:82.
[15] Suo Z. Adv Appl Mech 1997;33:193.
[16] Sevostianov I, Kachanov M, Ruud J, Lorraine P, Dubois M. Mater Sci Eng 2004;A386:164.
[17] Miller KT, Lange FF. Acta Metall 1989;37:1343.
[18] Sun B, Suo Z, Cocks ACF. J Mech Phys Solids 1996;44:559.
[19] Guo S, Kagawa Y. Scripta Mater 2004;50:1401.